Inorganic Chemistry

pubs.acs.org/IC Article

Toward Understanding Prolate 4f Monomers: Numerical Predictions and Experimental Validation of Electronic Properties and Slow Relaxation in a Muffin-Shaped Er^{III} Complex

Jan Arneth,*,[∥] Christian Pachl,[∥] Gerlinde Greif, Birte G. Beier, Peter W. Roesky,* Karin Fink,* and Rüdiger Klingeler*

Cite This: https://doi.org/10.1021/acs.inorgchem.5c05241 Read Online

ABSTRACT: We report the synthesis, crystal structure, and magnetic properties of the muffin-shaped complex $[Er(PPTMP)_2(H_2O)][OTf]_3$ (PPTMP = (4-(6-(1,10-phenanthrolin-2-yl)pyridin-2-yl)-1H-1,2,3-triazol-1-yl)methyl pivalate) (**1**). Complex **1** is shown to exhibit field-induced slow relaxation of the magnetization at $B = 0.1$ T via two distinct relaxation paths. Using tunable high-frequency/high-field electron paramagnetic resonance spectroscopy, we experimentally determine the effective g-factors and zero field splittings (ZFS) of the two energetically lowest Kramers doublets (KD). Our data reveal that the distorted muffin-shaped ligand field favors an $m \simeq \pm 9/2$ magnetic ground state, while the main contribution to the first excited KD at $\Delta_{1\rightarrow 2} = 780(5)$ GHz is suggested to be $m \simeq \pm 5/2$. The ground state g-tensor has generally an axial form but hosts significant transversal components, which we conclude to be the source of single molecule magnet (SMM)-silent behavior in zero field. Our findings are backed up by *ab initio* spin−orbit configuration interaction calculations showing excellent agreement with the experimental data and, in particular, highlight that the counterions should be included in the numerical modeling of the crystalline structure.

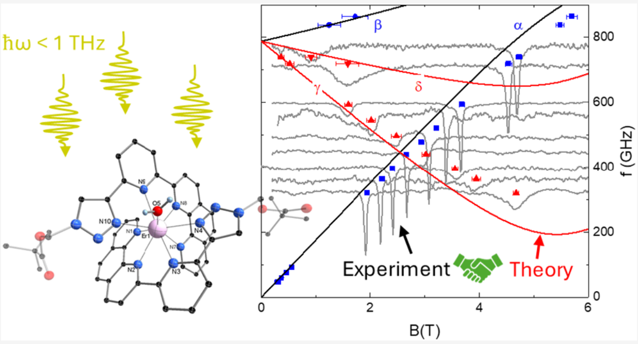

1. INTRODUCTION

The seminal paper by Sessoli et al. on the magnetic bistability in the famous dodecanuclear Mn_{12}ac-molecule[1] marked the birth of the ever-increasing research field centered around so-called single molecule magnets (SMM).[2−4] In SMM, the combination of large spins and strong magnetic anisotropy leads to high effective energy barriers (U_{eff}) due to which the magnetic moment relaxes only slowly and a remanent magnetization can be retained over long time scales below the blocking temperature T_B.[5] Therefore, such complexes have potential applications in quantum computing,[6] high-density information storage,[7] and novel molecular spintronic devices.[8,9]

On the route to high-performance SMM, 3d transition metal and 4f lanthanide ions have established themselves as the most promising building-blocks to realize high U_{eff} and T_B.[4,10] While the large spin and magnetic anisotropy of polynuclear 3d coordination clusters typically arise from strong ferromagnetic interactions between the distinct magnetic centers, 4f moments exhibit good magnetic relaxation properties due to intrinsically strong spin−orbit coupling and large unquenched orbital momentum.[3,11,12] Hence, almost 10 years after the discovery of Mn_{12}ac, Ishikawa et al. reported the first single-ion magnet (SIM) $[TbPc_2]^-$, in which slow magnetic relaxation occurs for a single terbium(III) in a double-decker coordination.[13] From there on, a vast amount of studies have been performed on 4f-based SIM and record barriers of $U_{eff} > 1800$ K[14] and magnetic hysteresis above liquid nitrogen temperatures $T_B = 100$ K[15] were achieved in this class of materials. However, despite huge zero field energy splittings, magnetic relaxation in SIM is often limited by under-barrier processes due to deviations from a perfectly axial crystal field. The resulting transversal magnetic anisotropy leads to a mixing of the m_J-levels which enables quantum tunneling of the magnetization (QTM) between energetically degenerate states.[16] Therefore, the choice of a suitable coordination environment for the central 4f ion is a key step in the effective design of a SIM.

In the literature, most of the reported SIM are based on the oblate 4f ions (Tb^{III}, Dy^{III}, Ho^{III}), while those with predominantly prolate electron distribution (Er^{III}, Tm^{III},

Received: November 7, 2025
Revised: January 13, 2026
Accepted: January 16, 2026

Scheme 1. Synthesis Scheme of Complex 1

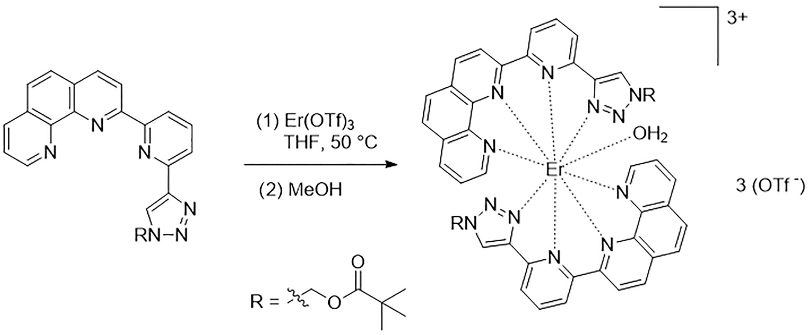

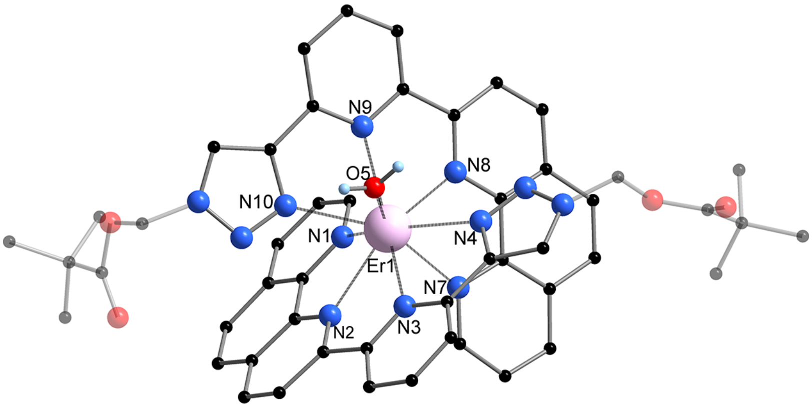

Figure 1. Molecular structure of the $[Er(PPTMP)_2(H_2O)]$-cation in the solid state. C−H-bound hydrogen atoms, solvent molecules, and uncoordinated triflate ions have been omitted for the sake of clarity.

Yb^{III}) rather scarcely exhibit slow relaxation of the magnetization.[17−24] This mainly results from the need for equatorial ligand fields to minimize the Coulomb interaction with the paramagnetic ion and, hence, to enhance the single-ion anisotropy, while still retaining a sufficient axiality.[25] However, this oblate versus prolate ion theory was demonstrated to be too simplified for the complex electronic structure of Er^{III} which renders trivalent erbium-based molecular complexes as interesting systems to investigate magnetic anisotropy in more detail.[17,26] Nonetheless, although a wide variety of Er^{III} complexes with different relaxation properties, i.e., SMM, field-induced SMM and completely SMM-silent, are known, quantitative analysis of the single-ion anisotropy is only rarely performed.

Here, we report the synthesis and magnetic characterization of the distorted muffin-shaped complex $[Er(PPTMP)_2(H_2O)][OTf]_3$ (PPTMP = (4-(6-(1,10-phenanthrolin-2-yl)pyridin-2-yl)-1H-1,2,3-triazol-1-yl)methyl pivalate) (**1**). Our ac susceptibility data show that **1** exhibits field-induced slow relaxation of the magnetization via two distinct relaxation pathways. We employ tunable high-frequency and high-field electron paramagnetic resonance (HF-EPR) spectroscopy which has been proven as a valuable method to study the magnetic anisotropy in Er^{III}-based molecular complexes by direct experimental determination of the effective *g*-factors and zero field splittings of the low-energy Kramers doublets (KD).[27,28] The spectroscopic data indicate that SMM-silent behavior in zero field arises from pronounced transverse components of the effective ground state *g*-tensor, while slow relaxation at finite fields occurs via an excited Kramers doublet at $\Delta_{1\rightarrow2}$ = 780 GHz. A direct comparison of our experimental findings with the numerical results of spin−orbit configuration interaction calculations using the CASOCI program[29] allows us to validate and assess *ab initio* predictions as recently done by us for various other mononuclear lanthanide complexes.[27,28,30,31]

2. RESULTS AND DISCUSSION

2.1. Structural Analysis

Reaction of PPTMP with erbium(III)-trifluoromethanesulfonate in THF led after workup to **1**. Single crystals suitable for X-ray diffraction were grown from hot methanol (Scheme 1). Compound **1** crystallizes in triclinic space group $P\bar{1}$ and contains two PPTMP-ligands coordinating the Er^{III} metal center. Figure 1 shows the molecular structure of the erbium complex in the solid state. The lanthanoid atom has a coordination number of nine, resulting from the coordination of eight nitrogen atoms from the two PPTMP ligands and one oxygen atom from a coordinated water molecule. This leads to a coordination geometry resembling a distorted muffin-shaped coordination polyhedron. In contrast, the three remaining triflate anions in the unit cell are not coordinating with the lanthanide ion.

In addition, the unit cell contains one noncoordinating methanol molecule which interacts with the Er-coordinated water molecule via a hydrogen bond. Furthermore, two of the three triflate anions also exhibit hydrogen bonds: one hydrogen bond toward the coordinated water molecule and the other toward the methanol molecule. The water molecule originates from the nondry solvents and the crystallization was not carried out in the absence of moisture and oxygen. The bond distances between the erbium atom and the coordinating nitrogen atoms are in the range of 2.473(2) to 2.510(2) Å. As already observed in similar and phenanthroline-pyridine ligand systems,[32−34] the nitrogen atoms N2 and N8 of the phenanthroline unit exhibit the shortest bond distances to the metal center with 2.473(2) Å each. The N−C bond lengths within the coordinated ligands also range from 1.327(3) to 1.373(3) Å, which is comparable with similar systems.[32−34]

2.2. Magnetometry

The static magnetic susceptibility $\chi = M/B$ of **1** in an external magnetic field of $B = 0.1$ T shown in Figure 2 by its $\chi T(T)$-profile is typical of mononuclear Er^{III} complexes.[19,35,36] At 300 K, the measured value of $\chi T = 10.71$ ergK/G^2 mol is close to the value of $\chi T_{\text{free}} = 11.48$ ergK/G^2 mol expected for a free Er^{III} ion. Since a sizable depletion due to crystal field effects is ruled out by the numerical calculations, as described later, the remaining discrepancy likely arises from solvent molecules cocrystallizing in the packing structure. Upon cooling, χT gradually decreases and then rapidly drops below 30 K which is attributed to the depopulation of the Stark levels. The isothermal magnetization at $T = 1.8$ K (inset of Figure 2) is characterized by a steep increase at low fields followed by a plateau-like behavior above 1 T. Up to the highest accessible field of 14 T, the magnetization gradually increases to M(14 T, 1.8 K) = 5.5 μ_B/f.u. (formula unit), i.e., does not reach the full saturation value ($M_{\text{sat}} = 9$ μ_B/f.u.), thereby confirming the presence of considerable magnetic anisotropy.

While complex **1** does not exhibit slow magnetic relaxation (up to 1 kHz) at $B = 0$ T, a clear out-of-phase ac susceptibility signal is found at low temperatures when a small static external field of $B_{\text{dc}} = 0.1$ T is applied (Figure S10a). From the frequency dependence of χ'' shown in Figure 3a, two maxima can be clearly discerned as confirmed by the appearance of two distinct lobes in the Cole−Cole plot (Figure 3b) and two step-like features in the $\chi'(f)$-profile (Figure S10b). Hence, the magnetization in **1** relaxes via two separate pathways with differing relaxation rates.[37,38] To corroborate our assignment, the ac susceptibility data were fitted by the sum of two generalized Debye-functions

$$\chi_{\text{ac}}(f) = \sum_{n=1}^{2}\left(\chi_{S,n} + \frac{\chi_{T,n} - \chi_{S,n}}{1 + (if\ \tau_n)^{1-\alpha_n}}\right) \tag{1}$$

where χ_S and χ_T denote the adiabatic and isothermal susceptibilities, τ is the relaxation time, and $0 \leq \alpha \leq 1$ qualitatively represents the distribution of relaxation times within the powder sample. As visible in Figure 3, the experimental data are well described by the model used. At 1.8 K, the shorter relaxation time $\tau_2 \simeq 3$ ms of the dominant relaxation pathway is comparable to findings in reported Er^{III}-based complexes exhibiting field-induced slow relaxation of the magnetization.[18,36,39−41] With increasing temperature, the features in χ_{ac} become less pronounced, and both relaxation processes occur at higher relaxation rates. This shift leads to significant uncertainties in the fit parameters for $T > 2.1$ K, i.e., when τ_2^{-1} exceeds the available frequency range, which limits a quantitative discussion of the relaxation times to low temperatures. The Arrhenius plot for τ_2 (inset of Figure 3a) can be described by an exponential behavior of the form $\tau = \tau_0 \exp(U_{\text{eff}}/k_B T)$ with $\tau_0 = 7.5 \times 10^{-8}$ s and $U_{\text{eff}} = 19.2$ K. It should be noted here that these parameters do not necessarily imply magnetic relaxation via an Orbach process, but they could also reflect alternative temperature-activated relaxation mechanisms, such as direct or Raman processes. The absence of SMM behavior in zero field straightforwardly implies a considerable transversal magnetic anisotropy acting on the Er^{III} moment. Such off-diagonal elements in the single-ion anisotropy tensor lead to a mixing of the m_J-states and, thus, give rise to fast QTM which can be effectively quenched by an external magnetic field.[16]

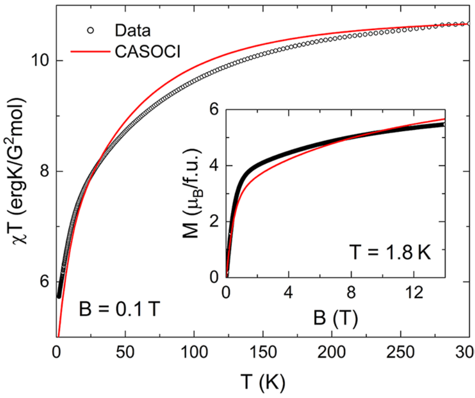

Figure 2. Temperature dependence of the χT-product at $B = 0.1$ T and isothermal magnetization at $T = 1.8$ K (inset) of **1**. Red lines depict the numerical results of *ab initio* CASOCI calculations for the full model (otf3) as described in Section 2.4.

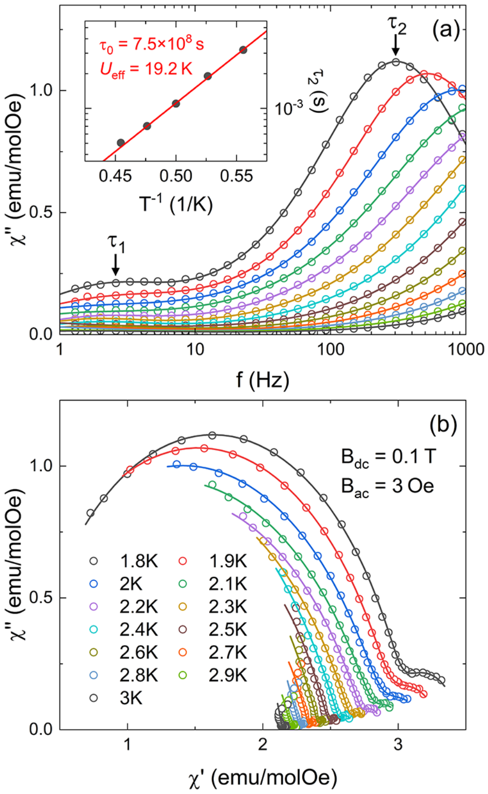

Figure 3. Out-of-phase ac susceptibility (a) and Cole−Cole plot (b) of **1** at selected temperatures and external static magnetic field B_{dc} = 0.1 T. Solid lines depict fits to the data using eq 1 as described in the text. Black arrows mark the two different relaxation times, τ_1 and τ_2. The inset in (a) shows the Arrhenius plot for τ_2 with a fit to the data, as described in the text.

2.3. High-Field EPR Studies

To experimentally probe the low-energy magnetic excitations in **1** and, in particular, to quantitatively determine the magnetic anisotropy, we performed multifrequency HF-EPR studies both on loose and fixed powders of freshly ground samples. The oriented loose powder HF-EPR spectra obtained at $T = 2$ K (Figure 4) display a pronounced Lorentzian-shaped absorption feature in the entire accessible frequency range up to 900 GHz. For frequencies higher than ca. 800 GHz, an additional weak broad resonance feature appears at smaller magnetic fields. The extracted resonance field positions at different frequencies are shown in Figure 4, too. As visualized by the solid black lines, the pronounced main feature forms a gapless resonance branch, here labeled as α, which exhibits linear field dependence at small magnetic fields but begins to deviate from its initial linear behavior for $B \gtrsim 4$ T. In agreement with the findings of the ac susceptibility studies and as further discussed below, the high-field bending of resonance branch α is associated with an avoided level crossing and, hence, indicates the mixing of different m_J-levels. Linear extrapolation of the two data points marking the weak low-field feature yields a tentative resonance branch β with a zero field splitting (ZFS) of $\Delta \simeq 780$ GHz. From the slopes of the observed resonance branches, we read off the effective g-factors $g_{\mathrm{eff}} \simeq 11.8$ and 3.2 for α and β, respectively.

The effect of temperature on the HF-EPR spectra is shown in Figure 5a at an exemplary frequency of $f = 593.9$ GHz. Upon heating, the spectral weight of the pronounced main feature corresponding to the resonance branch α gradually decreases until it becomes almost indiscernible around 50 K. Further, starting from $T \simeq 8$ K, an additional absorption peak (γ) appears in the spectra which first increases in intensity with rising temperature and then vanishes again for $T \geq 50$ K. To investigate the field dependence of γ, HF-EPR spectra at different frequencies were acquired at $T = 18$ K, i.e., where the resonance feature is most pronounced. As visible in the spectra and in the corresponding frequency-field diagram in Figure 5b, two additional resonance branches (γ and δ) are observed at elevated temperatures (for the full spectra up to 16 T see the SI). Similar to the behavior of α, γ follows a linear field dependence at small fields and exhibits significant bending at $B \gtrsim 4$ T. As will be discussed in detail below, this nonlinear field dependence further confirms the occurrence of state mixing in **1**. The zero field gaps of γ and δ, obtained by extrapolating the branches to $B = 0$ T, coincide with that of β within the error bars of our experiment.

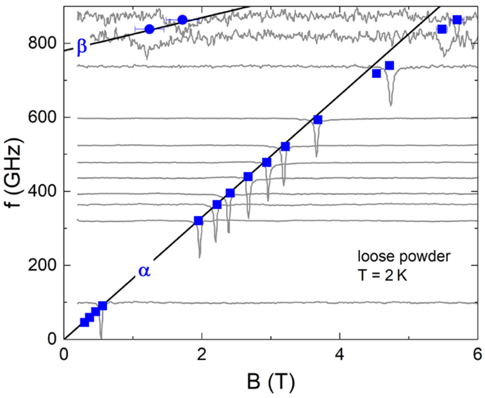

Figure 4. Resonance frequency versus magnetic field diagram for a loose powder sample of **1** obtained at $T = 2$ K. Blue squares mark the resonance positions as read off the measured HF-EPR spectra displayed in the background. Solid black lines depict simulations of the ground state resonance branches using a $S = 1/2$ pseudospin model for each KD as described in the text.

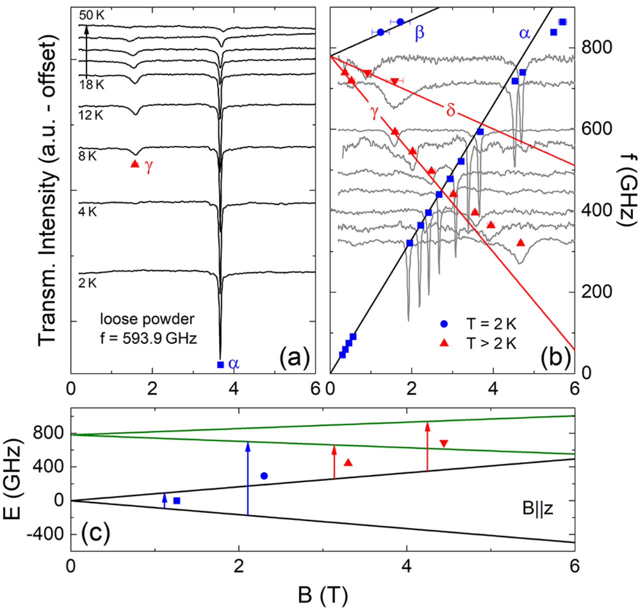

Figure 5. Loose powder HF-EPR spectra (shifted along the ordinate) of **1** at selected temperatures and at fixed frequency $f = 593.9$ GHz (a), the corresponding frequency-field diagram (b), and simulated energy levels of the two energetically lowest KDs (c). Solid black/red lines in panel (b) depict simulated ground/excited state transitions corresponding to the arrows in panel (c) which follow the same color scheme. Gray lines in the background of panel (b) display HF-EPR spectra measured at $T = 18$ K.

Due to the absence of a zero field excitation gap and its Curie-like temperature dependence, it is straightforward to attribute α to a transition within the energetically lowest Kramers doublet (KD1). In contrast, the observed finite ZFS of branches β-δ renders them likely to be associated with transitions between two distinct KDs. While the occurrence of β at $T = 2$ K implies the magnetic ground state (GS) to be its initial state, the temperature dependencies of γ and δ show that the corresponding transitions arise from thermally excited states (ES) a few K above the GS.

The observed resonance branches can be rationalized by assuming a $S = 1/2$ pseudospin model for the two energetically lowest KDs. The best simulations (solid lines in Figure 5b) are obtained using a zero field splitting of $\Delta_{1\rightarrow 2} = 780(5)$ GHz and effective g-factors of $g_{\mathrm{eff},1} = 11.8(1)$ and $g_{\mathrm{eff},2} = 5.4(3)$ for KD1 and KD2, respectively. As can be seen from the corresponding simulated Zeeman diagram in Figure 5c, the upward branch of KD1 and the downward branch of KD2 cross at $B \simeq 6$ T. While transverse components of the magnetic anisotropy tensor are effectively neglected in the $S = 1/2$ pseudospin model, their presence in the actual complex is clearly suggested by an avoided-level-crossing behavior which qualitatively explains the observed bending of branches α and γ.

Due to the alignment of the sample with the external magnetic field, the loose powder studies provide quantitative information only on the easy anisotropy direction of the studied complex. To determine also the transverse components of the effective g-tensor, we performed HF-EPR measurements on a fixed powder of **1**. Figure 6 displays the corresponding spectra obtained at $T = 2$ K for two exemplary frequencies in the V-band range (for a full spectrum up to 16 T see the SI).

https://doi.org/10.1021/acs.inorgchem.5c05241
Inorg. Chem. XXXX, XXX, XXX−XXX

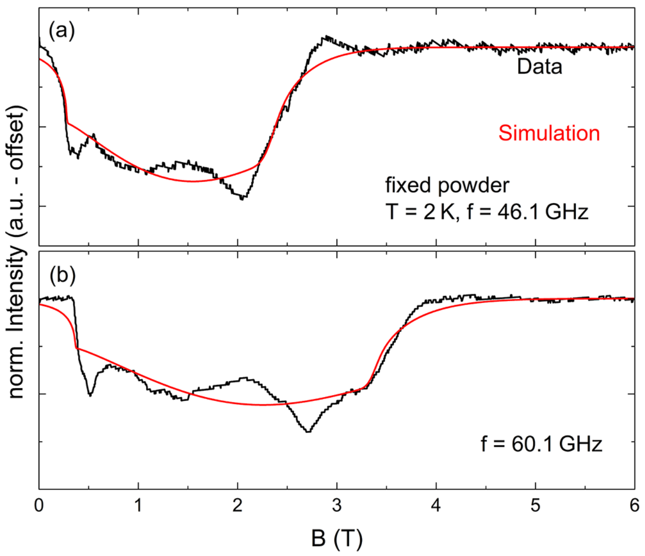

Figure 6. Measured (black) and simulated (red) fixed powder HF-EPR spectra of **1** at $T = 2$ K for $f = 46.1$ GHz (a) and $f = 60.1$ GHz (b).

The general shape of the low-temperature fixed powder HF-EPR spectra is given by a broad absorption minimum superimposed by several sharper (but in comparison to the resonances observed in the loose powder spectra very weak) resonance features. While the former is a typical characteristic of the measured powder average, the latter likely arises from clusters of crystallites that remained partially ordered after the loose powder measurements. The wide distribution of spectral weight straightforwardly indicates considerable transversal components of g_{eff} for KD1, i.e., a mixing of states due to off-diagonal crystal field parameters, which elucidates the absence of SMM behavior in **1** at $B = 0$ T. The components of g_{eff} can be quantified by fitting the overall shape of the spectra using a $S = 1/2$ pseudospin model with a strongly anisotropic g-tensor.[27,28,30] The best agreement with the experimental data is achieved by $g_{\mathrm{eff},x} = 1.4(2)$, $g_{\mathrm{eff},y} = 2.2(4)$, and $g_{\mathrm{eff},z} = 11.7(3)$ with anisotropic line broadening expressed in the g-strain parameters $\Delta g_{\mathrm{eff},x} = 0.1$, $\Delta g_{\mathrm{eff},y} = 0.4$, and $\Delta g_{\mathrm{eff},z} = 0.1$. The simulated spectra are shown as red lines in Figure 6.

2.4. Quantum Chemical Calculations

Using the workflow described in the experimental section, the electronic structure of **1** is solved by *ab initio* methods. In particular, we systematically investigated the influence of the counterions on the numerical results. The relevance of second-sphere effects in Er(III)-based compounds has been subject to recent discussion.[42,43] Considering the topological similarity of **1** to the well studied DOTA-compounds,[44] the influence of hydrogen-bridges and counterions is assumed to be important. Therefore, five model clusters are simulated: The first is the bare molecule, i.e., the cation, with a charge of +3 (named "bare" in Figure 7). Second, the MeOH hydrogen bound to the coordinating water is included, which remains in the charge state +3. Next, the three counterions are added sequentially yielding models "otf1" to "otf3" which, therefore, exhibit a charge of +2, +1, and 0, respectively. Pictures of the different model complexes can be found in the SI (Figure S12). Furthermore, calculations are carried out with and without a preliminary optimization of hydrogen positions. Lastly, an intermediate CASSCF step is tested for H-optimized models. This calculation has not been performed for the largest model due to an internal basis set limit. The resulting splitting of the $^4I_{15/2}$-ground state is visualized in Figure 7. The exact zero field splittings, diagonal elements of the g-tensors for each KD, extended Stevens operator equivalents, and m_J-compositions for all calculations are summarized in the Supporting Information.

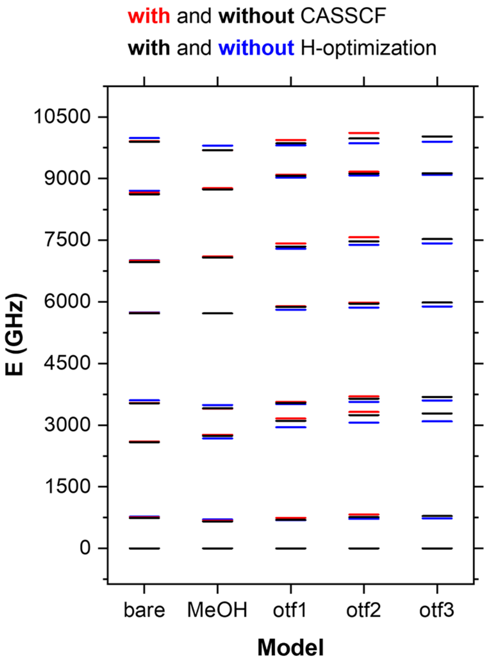

Figure 7. Calculated energies of the 8 lowest Kramers doublets of the $^4I_{15/2}$-ground state of complex **1** using various models from the bare cation molecule to the full asymmetric unit with three anions as described in the main text. Black: Energies with H-optimization and without an intermediate CASSCF step. Blue: Energies without H-optimization and without intermediate CASSCF step. Red: Energies with H-optimization and intermediate CASSCF step.

Our results show that neither the optimization of the hydrogen positions nor the inclusion of an intermediate CASSCF step significantly influences the calculated energy splittings. The observed differences between the respective models are smaller than 120 GHz for the zero field splitting of the first excited KD. The influence of including more counterions in the different model clusters is only marginally larger, as the lowest value of $\Delta_{1\rightarrow2} \simeq 650$ GHz is calculated for the model that includes MeOH and 790 GHz is found for the full model (otf3). The small differences in energy translate to weak discrepancies in the calculated g_z-values of the ground state KD, which are between 11.8 and 12.8 for all calculated models. A similar difference in absolute values can be reported for the transversal components of the g-tensor, with values ranging from 0.10 to 1.63 for g_x and from 0.89 to 2.71 for g_y. Thus, the inclusion of counterions is shown to notably influence the transversal components of the g-tensor and to significantly overestimate the anisotropy in some cases. The calculation considering the optimized H-positions, no intermediate CASSCF step and including all counterions, yields transversal g-tensor components of $g_x = 1.10$ and $g_y = 1.95$, which is in very good agreement with the experimental results.

The molecular magnetic easy axes, i.e., the g_z-direction of the ground state KD, calculated for all investigated models are shown in Figure 8. Independent of the used model, the magnetic easy axis lies orthogonal to the Er−O bond and is oriented through the two PPTMP ligands. In numbers, the angle between the Er−O bond and the ground state KD easy axis attains values between 86° and 90° for all models. A full list can be found in SI (Table S33). The maximum angle between the easy anisotropy axes of two different models is around 35°. Considering the prolate 4f electron distribution of Er^{III}, the magnetic easy anisotropy axis points in the direction of the minimal electrostatic field.[25] In **1**, the water molecule exerts the largest electrostatic field. Therefore, the magnetic easy axis lies orthogonal to the Er−O bond. Its orientation within the corresponding plane strongly depends on the model used. The analysis is corroborated by the molecular symmetry being close to C_2 which allows only for anisotropy axes parallel and perpendicular to the Er−O bond, which acts as the rotational axis. The χT-product and isothermal magnetization resulting from the numerical studies are exemplary, depicted in Figure 2, for the model including all counterions, optimized hydrogen positions, and no intermediate CASSCF calculation. The qualitatively same curve is obtained for all other models and is shown in the SI.

The comparison of the different computational models to the EPR spectra calls for a more detailed analysis of the obtained g-tensors. For example, for the first excited KD of the full optimized model without CASSCF, a g_z-value of 9.2 is calculated. This value is not directly comparable to the $g_{\mathrm{eff},z}$ obtained from the loose powder HF-EPR data since in the experiment, the crystallites are oriented along the main magnetic anisotropy axis of the ground state. The calculated effective $g_{\mathrm{eff},z}$, therefore, is given by the projection of the real g_z-value onto the magnetic field direction. This leads to $g_{\mathrm{eff},z} = 7.0$ for KD2. In comparison, the calculated and projected g_z-values for the bare molecules with and without optimizing the hydrogen positions are 1.8 and 2.7, respectively, which are far off the experimentally determined values. However, the calculated and projected g_z-value for the full model, without optimizing hydrogen positions, is 5.8 which is very close to the experimental value.

By applying a magnetic field in the direction of the ground state anisotropy axis, we are able to simulate the underlying Zeeman-diagrams for the loose powder EPR experiment, as shown exemplarily in Figure 9. The transition energies between the four lowest states can be directly compared with the experimental data in Figure 5. Figure 9 shows such a simulation for the full optimized model without an intermediate CASSCF step. The same analysis is done for all other models and depicted in SI. The accuracy of all models is reasonable and evaluated in terms of their R^2-value, Root Mean Square Deviation (RMSD), and Mean Absolute Errors (MAE). The best agreement with the loose powder HF-EPR data is found for the bare model without H-optimization. However, it fails to reproduce the observed avoided level crossing. In general, the agreement with the experiment becomes worse upon inclusion of the methanol solvent and improves again with the inclusion of counterions. In the following, we will hence discuss the model with optimized H-position, no CASSCF calculation, and all counterions. This model was chosen since, in agreement with the experiment, an avoided level crossing close to a field of 6 T with first deviations of the linear behavior starting at around 4 T is predicted. It also includes the largest amount of crystal space tested here and exhibits realistic hydrogen bond lengths.

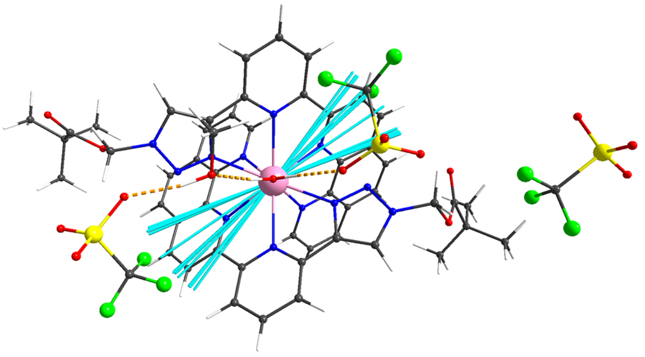

Figure 8. Orientation of the magnetic easy axes, for all investigated models, as indicated by the light blue lines. The underlying crystal field parameters are summarized in SI.

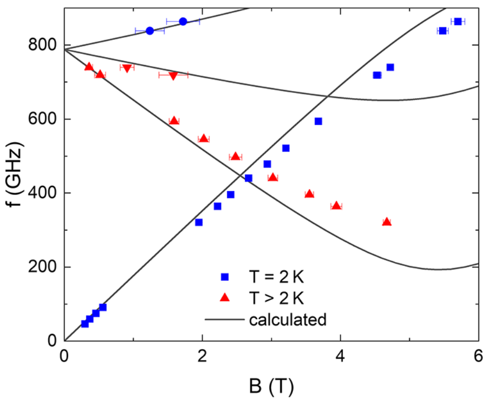

Figure 9. Measured (points) and calculated (lines) transition energies of a loose powder sample of **1** within the lowest two Kramers doublets for the model including all counterions and optimized hydrogen positions (otf3).

The mixing of m_J-states is calculated for the eight Kramers Doublets. The ground state is mainly a mixture of the $m_J = \pm 15/2 (\approx 31\%)$ and $m_J = \pm 9/2 (\approx 51\%)$ states. In contrast, the first excited state dominantly consists of the $m_J = \pm 7/2 (\approx 56\%)$ and $m_J = \pm 5/2 (\approx 22\%)$ states. These values are in good agreement with the experiment but depend on the model used to a certain extend. For example, using the bare molecule and no optimization of H-positions will lead to a ground state that is a mixture of $m_J = \pm 15/2$, 9/2 and 5/2 with 26, 33, and 20%, respectively, while the first excited state is an equal mixture of the $m_J = \pm 7/2$, 3/2, and 1/2 states with contributions between 24 and 28%. In summary, the comparison of the different models shows that the methanol as well as the three counterions should be considered to obtain the correct magnetic axes and g-values, while the energy differences are already well described by modeling only the bare molecule.

2.5. Discussion

A summary of the effective g-tensors and crystal field splittings as obtained by the HF-EPR measurements and the *ab initio* calculations is given in Table 1. Our experimental and theoretical results clearly evidence a pronounced uniaxial behavior, i.e., $g_{\mathrm{eff},z} \gg g_{\mathrm{eff},x}, g_{\mathrm{eff},y}$, of the energetically lowest Kramers doublet in **1** and, hence, imply an Ising-like character of the Er^{III} moment in the magnetic ground state. According to the calculations, the water ligand is responsible for the largest

Table 1. Experimentally and Theoretically Obtained Effective g-Tensors and Zero Field Splittings of the Two Lowest KDs in **1**[a]

		HF-EPR	CASOCI
	$g_{\mathrm{eff},x}$	1.4(2)	1.1
KD1	$g_{\mathrm{eff},y}$	2.2(4)	2.0
	$g_{\mathrm{eff},z}$	11.8(1)	12.6
$\Delta_{1\to2}$ (GHz)		780(5)	788
KD2	$g_{\mathrm{eff},z}$	5.4(3)	7.0
$\Delta_{2\to3}$ (GHz)		$\gg$1000	2495

[a] The theoretical model including all counterions, optimized H-positions, and using ROHF to obtain the starting orbitals for CASOCI.

contribution to the ligand field, therefore the direction of the Ising-axis is perpendicular to it. However, the observation of sizable $g_{\mathrm{eff},x/y}$ components in the effective g-tensor directly reveals a significant deviation from a perfect Ising scenario due to the presence of a considerable transversal crystal field.

The large off-diagonal elements of the ground state g-tensor are responsible for the observed fast QTM. This can be shown for example with the model of Yin et al. based on time-dependent perturbation theory[45,46] or by the model of Prokof'ev and Stamp rooted in instanton theory.[47−49] Employing these models predicts tunneling times (without an external applied field) well below experimental resolution in the order of 10^{-8} s. This is corroborated by large magnetic transition moments calculated for the ground state KD. The obtained numbers are comparable for all models and can be found in SI.

The presence of sizable off-diagonal elements in the single-ion anisotropy tensor and the associated mixing of the m_J states straightforwardly explains the observed avoided level crossings and fast magnetic relaxation via QTM in zero field. As demonstrated by the ac susceptibility data, the QTM in **1** can be effectively quenched by shifting the energy levels of the initial and final states using a small magnetic field. In this in-field configuration, magnetic relaxation is dominated by temperature-activated processes, such as Orbach, Raman, or thermally assisted QTM. While KD3 is strongly gapped $\Delta_{2\to3} \gg 1$ THz, the first excited Kramers doublet KD2 lies approximately 37 K (780 GHz) above the ground state and can easily contribute to the observed slow magnetic relaxation.

The effective g-factors obtained from the pseudosingle-crystal loose powder spectra can be used to determine the effective magnetic quantum numbers $m_{\mathrm{eff}} = g_{\mathrm{eff},z}/2g_L$ for the experimentally accessible Kramers doublets.[27,28] Assuming that the free ion Landé factor $g_L = 1.2$ is still a good approximation for Er^{III} moments in the present coordination geometry, our analysis yields $m_{\mathrm{eff},1} = 4.9(1)$ and $m_{\mathrm{eff},2} = 2.3(1)$ for KD1 and KD2, respectively. The almost integer value of $m_{\mathrm{eff},1}$ for KD1 confirms the occurrence of pronounced state mixing, as also evidenced by the observation of avoided level crossing in the frequency-field diagram. Furthermore, $m_{\mathrm{eff},1}$ is close to 4.5, which indicates that the low-symmetry crystal field in **1** stabilizes the $m_J = \pm 9/2$ state as the magnetic ground state. As for KD2, the main contribution to the spin wave function is suggested to be $m_J = \pm 5/2$.

As already evident from the good agreement of the measured and calculated dc magnetization, the experimentally determined g-tensor for KD1 is well reproduced by CASOCI. While CASOCI also gives an accurate prediction of the zero field gap to the first excited Kramers doublet, the effective g_z-value for KD2 is slightly overestimated by this approach. In agreement with the absence of corresponding transitions in the HF-EPR experiments, the calculation finds KD3 to be strongly gapped with $\Delta_{2\to3} \simeq 2.5$ THz, i.e., well beyond the experimentally accessible range.

To obtain this good agreement with the experimental data, more counterions were progressively included in our calculations. While all tested models give reasonable results, a balanced extension of the chemical model into the crystal space is needed to obtain the best agreement with HF-EPR. The model using correct bond distances for H and including the largest crystal space yields the best agreement with experiment by reproducing the avoided level crossing at around 6 T. It is suggested that a study of the chemical model may be advantageous for future calculations on low-symmetry Er-SMMs to disentangle second-sphere effects. In this case, HF-EPR and *ab initio* calculations prove to be a powerful combination to investigate the electronic structure of compound **1**.

3. CONCLUSIONS

To sum up, we successfully synthesized and magnetically characterized a distorted muffin-shaped Er^{III} complex **1** using combined dc and ac magnetic, HF-EPR, and numerical studies. Complex **1** is SMM-silent due to QTM in zero field, but exhibits field-induced slow relaxation of the magnetization at $B = 0.1$ T. The dominance of under-barrier relaxation is rationalized by the presence of sizable transversal components in the overall uniaxial effective g-tensor of the ground state KD1. When the QTM is quenched, slow magnetic relaxation happens via thermally activated processes involving the first excited KD2 at 780 GHz above the ground state. KD3 is shown to be strongly gapped and thus does not contribute to the relaxation dynamics at low temperatures. In particular, our detailed spectroscopic investigations allow for a direct experimental determination of the effective g-tensors and zero field splittings of the two energetically lowest Kramers doublets. While the excellent agreement between the measured data and the results of the CASOCI calculations for g-tensors and zero field splitting support the reliability of both approaches, our systematic numerical analysis of different models also implies that the inclusion of the counterions by means of a balanced extension of the chemical model is needed for optimal computational results.

4. EXPERIMENTAL SECTION

Polycrystalline powder samples of **1** have been synthesized as described in the Supporting Information.

For crystal structure determination, a suitable crystal of **1** was covered in mineral oil (Aldrich) and mounted on a glass fiber. The crystal was transferred directly to the cold stream of a STOE StadiVari (100 K) diffractometer. All structures were solved by using the program SHELXS/T[50,51] and Olex.[52] The remaining non-hydrogen atoms were located from successive difference Fourier map calculations. The refinements were carried out by using full-matrix least-squares techniques on F^2 by using the program SHELXL.[50,51] The H atoms were introduced into the geometrically calculated positions (SHELXL procedures) unless otherwise stated and refined by riding on the corresponding parent atoms. In each case, the locations of the largest peaks in the final difference Fourier map calculations as well as the magnitude of the residual electron densities were of no chemical significance. Summary of the crystal data, data collection, and refinement for compounds are given in the supplement. Crystallographic data for the structures reported in this paper have been deposited with the Cambridge Crystallographic Data Centre as a supplementary publication no. CCDC 2472872. Copies of the data can be obtained free of charge on application to CCDC, 12 Union Road, Cambridge CB21EZ, U.K. (fax: (+(44)1223-336-033); email: deposit@ccdc.cam.ac.uk). The coordination geometry of Er^{III} ions was calculated using the SHAPE 2.1 software.[53]

The direct current (dc) and alternating current (ac) magnetization was studied in the temperature range $T = 1.8$−300 K by means of a Magnetic Properties Measurement System (MPMS3, Quantum Design) and a Physical Properties Measurement System (PPMS, Quantum Design) in magnetic fields up to 7 and 14 T, respectively. For all measurements, powder samples were pelletized in polycarbonate capsules to avoid reorientation in external magnetic fields. The experimental data were corrected for the contribution of the sample holder and of the diamagnetic ligand field calculated by means of Pascal's constants.[54] Simulations of the magnetic data were performed using the PHI software package.[55]

Tunable continuous wave high-frequency/high-field electron paramagnetic resonance studies were performed using a phase-sensitive millimeter vector network analyzer (MVNA) by ABmm as a simultaneous microwave source and detector.[30] The spectra were obtained by simultaneously measuring the transmitted microwave amplitude and phase at frequencies ranging from 40 to 850 GHz. All spectra were corrected for phase mixing and background effects, such as temperature drifts and contributions from the experimental setup.[56,57] Temperature control from 2 to 300 K in magnetic fields up to 16 T was ensured by placing the sample space in the Variable Temperature Insert (VTI) of an Oxford magnet system equipped with a Nb_3Sn superconducting coil.[58] Polycrystalline powder samples were prepared in a brass ring sealed with kapton tape either as loose powder or fixed by mixing with n-eicosane ($C_{20}H_{42}$, CAS Nr. 112-95-8). The former setup allows alignment of the crystallites with the external magnetic field, hence providing simplified pseudosingle-crystal spectra (see refs 27,28,59−62). Alignment is ensured by sweeping up the magnetic field to 16 T prior to each measurement and confirmed by observation of corresponding orientation effects in the transmitted microwave intensity signal. Spectral simulations of the HF-EPR data were performed using the EasySpin software package.[63]

Ab-initio Complete Active Space Spin−orbit Configuration Interaction (CASOCI) calculations[29] are carried out in the following steps: First, the hydrogen positions of the experimentally determined structure are optimized on a B3-LYP-d4/def2-TZVP[64−66] level of theory in TURBOMOLE,[67,68] by replacing Er to Y. For each model complex investigated, Y is replaced back to Er equipped with a x2c-TZVPall basis and the orbitals optimized with Restricted Open-Shell Hartree−Fock (ROHF). Scalar relativistic effects are accounted for at the DKH4 level of theory.[69,70] More details on this multistep-procedure can be found in SI. We have tested the influence of a subsequent state averaged CASSCF calculation for optimizing the orbitals explicitly for the ^{4}I-ground term using the wavels package.[71] Afterward, the CASOCI calculations were carried out explicitly introducing spin−orbit coupling. This is done by diagonalizing the spin−orbit coupled Full CI matrix in an active space of 11 electrons in the seven 4f orbitals (11,7) active space using a Davidson algorithm to extract the lowest 100 eigenstates.[29]

■ ASSOCIATED CONTENT

Data Availability Statement

The data underlying the quantum chemical calculations are openly available in KIT Open at 10.35097/sqa8baap3hheb278. Experimental data is available on request from the corresponding author.

Supporting Information

The Supporting Information is available free of charge at https://pubs.acs.org/doi/10.1021/acs.inorgchem.5c05241.

The Supplemental Information contains further details about the synthesis; structure figures and X-ray crystallographic data; NMR, IR, mass spectroscopy data; full HF-EPR spectra; and more information on numerical results. It also includes ref 72 and 73. Further information about the numerical results (PDF)

In addition, it includes xyz-files on all model structures used in this manuscript. The difference between optimized and unoptimized is that in optimized structures, hydrogen positions were optimized on a DFT level as described in the text. This was done considering all counterions and lattice solvent, so on the "full" structure. Afterward, the model was truncated to generate the other structures (ZIP)

Accession Codes

Deposition Number 2472872 contains the supplementary crystallographic data for this paper. These data can be obtained free of charge via the joint Cambridge Crystallographic Data Centre (CCDC) and Fachinformationszentrum Karlsruhe Access Structures service.

■ AUTHOR INFORMATION

Corresponding Authors

Jan Arneth − *Kirchhoff Institute for Physics, Heidelberg University, D-69120 Heidelberg, Germany;* orcid.org/0000-0002-1527-8449; Email: jan.arneth@kip.uni-heidelberg.de

Peter W. Roesky − *Institute of Inorganic Chemistry, Karlsruhe Institute of Technology, 76131 Karlsruhe, Germany;* orcid.org/0000-0002-0915-3893; Email: roesky@kit.edu

Karin Fink − *Institute of Nanotechnology, Karlsruhe Institute of Technology (KIT), 76131 Karlsruhe, Germany;* Email: karin.fink@kit.edu

Rüdiger Klingeler − *Kirchhoff Institute for Physics, Heidelberg University, D-69120 Heidelberg, Germany;* Email: klingeler@kip.uni-heidelberg.de

Authors

Christian Pachl − *Institute of Nanotechnology, Karlsruhe Institute of Technology (KIT), 76131 Karlsruhe, Germany; Institute of Inorganic Chemistry, Karlsruhe Institute of Technology, 76131 Karlsruhe, Germany;* orcid.org/0009-0005-8105-0409

Gerlinde Greif − *Institute of Inorganic Chemistry, Karlsruhe Institute of Technology, 76131 Karlsruhe, Germany*

Birte G. Beier − *Kirchhoff Institute for Physics, Heidelberg University, D-69120 Heidelberg, Germany*

Complete contact information is available at: https://pubs.acs.org/10.1021/acs.inorgchem.5c05241

Author Contributions

‖J.A. and C.P. contributed equally to this work.

Notes

The authors declare no competing financial interest.
A preprint of this article was uploaded to arXiv.[74]

■ ACKNOWLEDGMENTS

We thank Florian Bruder and Florian Weigend for valuable discussions and scientific input. David Frick is acknowledged for solving the single crystal X-ray structure of compound **1**.

Support by Deutsche Forschungsgemeinschaft (DFG) under Germany's Excellence Strategy EXC2181/1-390900948 (the Heidelberg STRUCTURES Excellence Cluster) is gratefully acknowledged. J.A. acknowledges support by the International Max-Planck Research School for Quantum Dynamics (IMPRS-QD) Heidelberg. Financial support for this research was provided by the German Federal Ministry of Education and Research through the f-Char and CORDEX projects under grant numbers 02NUK059A and 02NUK103D. C.P. acknowledges the state of Baden-Württemberg via the Landesgraduiertenförderung and the DFG via the CRC 1573 "4f for future" for funding.

■ REFERENCES

(1) Sessoli, R.; Gatteschi, D.; Caneschi, A.; Novak, M. A. Magnetic bistability in a metal-ion cluster. *Nature* **1993**, *365*, 141−143.

(2) Christou, G.; Gatteschi, D.; Hendrickson, D. N.; Sessoli, R. Single-Molecule Magnets. *MRS Bull.* **2000**, *25*, 66−71.

(3) Sessoli, R.; Powell, A. K. Strategies towards single molecule magnets based on lanthanide ions. *Coord. Chem. Rev.* **2009**, *253*, 2328−2341.

(4) Shao, D.; Wang, X. Development of Single-Molecule Magnets. *Chin. J. Chem.* **2020**, *38*, 1005−1018.

(5) Winpenny, R., Ed. *Single-Molecule Magnets and Related Phenomena*; Springer: Berlin Heidelberg, 2006.

(6) Shiddiq, M.; Komijani, D.; Duan, Y.; Gaita-Ariño, A.; Coronado, E.; Hill, S. Enhancing coherence in molecular spin qubits via atomic clock transitions. *Nature* **2016**, *531*, 348−351.

(7) Coronado, E. Molecular magnetism: from chemical design to spin control in molecules, materials and devices. *Nat. Rev. Mater.* **2020**, *5*, 87−104.

(8) Sanvito, S. The rise of spinterface science. *Nat. Phys.* **2010**, *6*, 562−564.

(9) Sanvito, S. Molecular spintronics. *Chem. Soc. Rev.* **2011**, *40*, 3336.

(10) Vieru, V.; Gómez-Coca, S.; Ruiz, E.; Chibotaru, L. F. Increasing the Magnetic Blocking Temperature of Single-Molecule Magnets. *Angew. Chem.* **2023**, *136*, No. e202303146.

(11) Sorace, L.; Benelli, C.; Gatteschi, D. Lanthanides in molecular magnetism: old tools in a new field. *Chem. Soc. Rev.* **2011**, *40*, 3092.

(12) Liddle, S. T.; van Slageren, J. Improving f-element single molecule magnets. *Chem. Soc. Rev.* **2015**, *44*, 6655−6669.

(13) Ishikawa, N.; Sugita, M.; Ishikawa, T.; Koshihara, S.; Kaizu, Y. Lanthanide Double-Decker Complexes Functioning as Magnets at the Single-Molecular Level. *J. Am. Chem. Soc.* **2003**, *125*, 8694−8695.

(14) Zhu, Z.; Zhao, C.; Feng, T.; Liu, X.; Ying, X.; Li, X.-L.; Zhang, Y.-Q.; Tang, J. Air-Stable Chiral Single-Molecule Magnets with Record Anisotropy Barrier Exceeding 1800 K. *J. Am. Chem. Soc.* **2021**, *143*, 10077−10082.

(15) Emerson-King, J.; Gransbury, G. K.; Atkinson, B. E.; Blackmore, W. J. A.; Whitehead, G. F. S.; Chilton, N. F.; Mills, D. P. Soft magnetic hysteresis in a dysprosium amide−alkene complex up to 100 K. *Nature* **2025**, *643*, 125−129.

(16) Thomas, L.; Lionti, F.; Ballou, R.; Gatteschi, D.; Sessoli, R.; Barbara, B. Macroscopic quantum tunnelling of magnetization in a single crystal of nanomagnets. *Nature* **1996**, *383*, 145−147.

(17) Brown, A. J.; Pinkowicz, D.; Saber, M. R.; Dunbar, K. R. A Trigonal-Pyramidal Erbium(III) Single-Molecule Magnet. *Angew. Chem.* **2015**, *127*, 5962−5966.

(18) Gorczyński, A.; Kubicki, M.; Pinkowicz, D.; Pełka, R.; Patroniak, V.; Podgajny, R. The first example of erbium triple-stranded helicates displaying SMM behaviour. *Dalton Trans.* **2015**, *44*, 16833−16839.

(19) Zhang, H.; Nakanishi, R.; Katoh, K.; Breedlove, B. K.; Kitagawa, Y.; Yamashita, M. Low coordinated mononuclear erbium(III) single-molecule magnets with C_{3v} symmetry: a method for altering single-molecule magnet properties by incorporating hard and soft donors. *Dalton Trans.* **2018**, *47*, 302−305.

(20) Castellanos, E.; Benner, F.; Demir, S. Linear, Electron-Rich Erbium Single-Molecule Magnet with Dibenzocyclooctatetraene Ligands. *Inorg. Chem.* **2024**, *63*, 9888−9898.

(21) Gavrikov, A. V.; Efimov, N. N.; Ilyukhin, A. B.; Dobrokhotova, Z. V.; Novotortsev, V. M. Yb^{3+} can be much better than Dy^{3}: SMM properties and controllable self-assembly of novel lanthanide 3,5-dinitrobenzoate-acetylacetonate complexes. *Dalton Trans.* **2018**, *47*, 6199−6209.

(22) Guégan, F.; Jung, J.; Le Guennic, B.; Riobé, F.; Maury, O.; Gillon, B.; Jacquot, J.-F.; Guyot, Y.; Morell, C.; Luneau, D. Evidencing under-barrier phenomena in a Yb(III) SMM: a joint luminescence/neutron diffraction/SQUID study. *Inorg. Chem. Front.* **2019**, *6*, 3152−3157.

(23) Jain, N.; Houard, F.; Marchal, R.; Cordier, M.; Le Guennic, B.; Suffren, Y.; Sarazin, Y.; Bernot, K. Luminescence and Single-Molecule Magnet Properties in Ideal Symmetry Compounds: Example of a Near-Planar Tricoordinate Ytterbium(III) Amide. *ChemistryEurope* **2024**, *2*, No. e202400062, DOI: 10.1002/ceur.202400062.

(24) Schwarz, N.; Bruder, F.; Bayer, V.; Moreno-Pineda, E.; Gillhuber, S.; Sun, X.; van Slageren, J.; Weigend, F.; Roesky, P. W. Rare earth stibolyl and bismolyl sandwich complexes. *Nat. Commun.* **2025**, *16*, No. 983, DOI: 10.1038/s41467-024-55474-6.

(25) Rinehart, J. D.; Long, J. R. Exploiting Single-Ion Anisotropy in the Design of f-Element Single-Molecule Magnets. *Chem. Sci.* **2011**, *2*, 2078.

(26) Lucaccini, E.; Sorace, L.; Perfetti, M.; Costes, J.-P.; Sessoli, R. Beyond the anisotropy barrier: slow relaxation of the magnetization in both easy-axis and easy-plane Ln(trensal) complexes. *Chem. Commun.* **2014**, *50*, 1648−1651.

(27) Spillecke, L.; Koo, C.; Maximova, O.; Mironov, V. S.; Kopotkov, V. A.; Korchagin, D. V.; Vasiliev, A. N.; Yagubskii, E. B.; Klingeler, R. Magnetic behavior of the novel pentagonal-bipyramidal erbium(III) complex $(Et_3NH)[Er(H_2DAPS)Cl_2]$: high-frequency EPR study and crystal-field analysis. *Dalton Trans.* **2021**, *50*, 18143−18154.

(28) Arneth, J.; Spillecke, L.; Koo, C.; Bazhenova, T. A.; Yagubskii, E. B.; Klingeler, R. The Relevance of Non-Axiality and Low-Lying Excited States for Slow Magnetic Relaxation in Pentagonal-Bipyramidal Erbium(III) Complexes Probed by High-frequency EPR. *Chem. - Eur. J.* **2025**, *31*, No. e202500369, DOI: 10.1002/chem.202500369.

(29) Bodenstein, T.; Heimermann, A.; Fink, K.; van Wüllen, C. Development and Application of a Complete Active Space Spin-Orbit Configuration Interaction Program Designed for Single Molecule Magnets. *ChemPhysChem* **2022**, *23*, No. e202100648.

(30) Comba, P.; Großhauser, M.; Klingeler, R.; Koo, C.; Lan, Y.; Müller, D.; Park, J.; Powell, A.; Riley, M. J.; Wadepohl, H. Magnetic Interactions in a Series of Homodinuclear Lanthanide Complexes. *Inorg. Chem.* **2015**, *54*, 11247−11258.

(31) Comba, P.; Daumann, L. J.; Klingeler, R.; Koo, C.; Riley, M. J.; Roberts, A. E.; Wadepohl, H.; Werner, J. Correlation of Structural and Magnetic Properties in a Set of Mononuclear Lanthanide Complexes. *Chem. - Eur. J.* **2018**, *24*, 5319−5330.

(32) Schnaubelt, L.; Petzold, H.; Speck, J. M.; Dmitrieva, E.; Rosenkranz, M.; Korb, M. Redox properties and electron transfer in a triarylamine-substituted $HS-Co^{2+}/LS-Co^{3+}$ redox couple. *Dalton Trans.* **2017**, *46*, 2690−2698.

(33) Petzold, H.; Djomgoue, P.; Hörner, G.; Heider, S.; Lochenie, C.; Weber, B.; Rüffer, T.; Schaarschmidt, D. Spin state variability in Fe^{2+} complexes of substituted (2-(pyridin-2-yl)-1,10-phenanthroline) ligands as versatile terpyridine analogues. *Dalton Trans.* **2017**, *46*, 6218−6229.

(34) Petzold, H.; Djomgoue, P.; Hörner, G.; Lochenie, C.; Weber, B.; Rüffer, T. Bis-meridional Fe^{2+} spincrossover complexes of phenyl and pyridyl substituted 2-(pyridin-2-yl)-1,10-phenanthrolines. *Dalton Trans.* **2018**, *47*, 491−506.

(35) Rechkemmer, Y.; Fischer, J. E.; Marx, R.; Dörfel, M.; Neugebauer, P.; Horvath, S.; Gysler, M.; Brock-Nannestad, T.; Frey, W.; Reid, M. F.; van Slageren, J. Comprehensive Spectroscopic

Determination of the Crystal Field Splitting in an Erbium Single-Ion Magnet. *J. Am. Chem. Soc.* **2015**, *137*, 13114−13120.

(36) Bazhenova, T. A.; Kopotkov, V. A.; Korchagin, D. V.; Manakin, Y. V.; Zorina, L. V.; Simonov, S. V.; Yakushev, I. A.; Mironov, V. S.; Vasiliev, A. N.; Maximova, O. V.; Yagubskii, E. B. A Series of Novel Pentagonal-Bipyramidal Erbium(III) Complexes with Acyclic Chelating N_3O_2 Schiff-Base Ligands: Synthesis, Structure, and Magnetism. *Molecules* **2021**, *26*, No. 6908.

(37) Davidson, D. W.; Cole, R. H. Dielectric Relaxation in Glycerol, Propylene Glycol, and n-Propanol. *J. Chem. Phys.* **1951**, *19*, 1484−1490.

(38) Havriliak, S.; Negami, S. A complex plane representation of dielectric and mechanical relaxation processes in some polymers. *Polymer* **1967**, *8*, 161−210.

(39) Gorczyński, A.; Marcinkowski, D.; Kubicki, M.; Löffler, M.; Korabik, M.; Karbowiak, M.; Wiśniewski, P.; Rudowicz, C.; Patroniak, V. New field-induced single ion magnets based on prolate Er(III) and Yb(III) ions: tuning the energy barrier U_{eff} by the choice of counterions within an N_3-tridentate Schiff-base scaffold. *Inorg. Chem. Front.* **2018**, *5*, 605−618.

(40) Liu, C.; Li, M.; Zhang, Y.; Tian, H.; Chen, Y.; Wang, H.; Dou, J.; Jiang, J. Controlling the Crystal Field of Heteroleptic Bis(phthalocyaninato) Erbium for Field-Induced Magnetic Relaxation. *Eur. J. Inorg. Chem.* **2019**, *2019*, 2940−2946.

(41) Casanovas, B.; Porcar, O.; Speed, S.; Vicente, R.; Font-Bardía, M.; El Fallah, M. S. Field-Induced SMM and Vis/NIR Luminescence on Mononuclear Lanthanide Complexes with 9-Anthracenecarboxylate and 2,2′:6,2″-Terpyridine. *Magnetochemistry* **2021**, *7*, No. 124.

(42) Herchel, R.; Zoufalý, P.; Nemec, I. The Effect of the Second Coordination Sphere on the Magnetism of $[\mathrm{Ln(NO_3)_3\,(H_2\,O)_3}]\cdot$(18-Crown-6) (Ln = Dy and Er). *RSC Adv.* **2019**, *9*, 569−575.

(43) Matheson, B. E.; Dais, T. N.; Donaldson, M. E.; Rowlands, G. J.; Plieger, P. G. The Importance of Second Sphere Interactions on Single Molecule Magnet Performance. *Inorg. Chem. Front.* **2023**, *10*, 6427−6439.

(44) Briganti, M.; Lucaccini, E.; Chelazzi, L.; Ciattini, S.; Sorace, L.; Sessoli, R.; Totti, F.; Perfetti, M. Magnetic Anisotropy Trends along a Full 4f-Series: The Fn+7 Effect. *J. Am. Chem. Soc.* **2021**, *143*, 8108−8115.

(45) Yin, B.; Li, C.-C. A Method to Predict Both the Relaxation Time of Quantum Tunneling of Magnetization and the Effective Barrier of Magnetic Reversal for a Kramers Single-Ion Magnet. *Phys. Chem. Chem. Phys.* **2020**, *22*, 9923−9933.

(46) Yin, B.; Luo, L. The Anisotropy of the Internal Magnetic Field on the Central Ion Is Capable of Imposing Great Impact on the Quantum Tunneling of Magnetization of Kramers Single-Ion Magnets. *Phys. Chem. Chem. Phys.* **2021**, *23*, 3093−3105.

(47) Prokof'ev, N. V.; Stamp, P. C. E. Quantum Relaxation of Magnetisation in Magnetic Particles. *J. Low Temp. Phys.* **1996**, *104*, 143−209.

(48) Prokof'ev, N. V.; Stamp, P. C. E. Theory of the Spin Bath. *Rep. Prog. Phys.* **2000**, *63*, 669−726.

(49) Luis, F.; Martínez-Pérez, M. J.; Montero, O.; Coronado, E.; Cardona-Serra, S.; Martí-Gastaldo, C.; Clemente-Juan, J. M.; Sesé, J.; Drung, D.; Schurig, T. Spin-Lattice Relaxation via Quantum Tunneling in an $\mathrm{Er^{3+}}$-Polyoxometalate Molecular Magnet. *Phys. Rev. B* **2010**, *82*, No. 060403.

(50) Sheldrick, G. M. A short history of SHELX. *Acta Crystallogr., Sect. A: Found. Crystallogr.* **2008**, *64*, 112−122.

(51) Sheldrick, G. M. Crystal structure refinement with SHELXL. *Acta Crystallogr., Sect. C: Struct. Chem.* **2015**, *71*, 3−8.

(52) Dolomanov, O. V.; Bourhis, L. J.; Gildea, R. J.; Howard, J. A. K.; Puschmann, H. OLEX2: a complete structure solution, refinement and analysis program. *J. Appl. Crystallogr.* **2009**, *42*, 339−341.

(53) Llunell, M.; Casanova, D.; Cirera, J.; Alemany, P.; Alvarez, S. *SHAPE*; Shape Software: Barcelona, Spain, 2013.

(54) Bain, G. A.; Berry, J. F. Diamagnetic Corrections and Pascal's Constants. *J. Chem. Educ.* **2008**, *85*, 532.

(55) Chilton, N. F.; Anderson, R. P.; Turner, L. D.; Soncini, A.; Murray, K. S. PHI: A powerful new program for the analysis of anisotropic monomeric and exchange-coupled polynuclear *d*- and *f*-block complexes. *J. Comput. Chem.* **2013**, *34*, 1164−1175.

(56) Feher, G.; Kip, A. F. Electron Spin Resonance Absorption in Metals. I. Experimental. *Phys. Rev.* **1955**, *98*, 337−348.

(57) Linzer, M. Line Parameters of Lorentzian Curves Containing Arbitrary Mixtures of Absorption and Dispersion. *J. Appl. Phys.* **1969**, *40*, 372−376.

(58) Werner, J.; Hergett, W.; Gertig, M.; Park, J.; Koo, C.; Klingeler, R. Anisotropy-governed competition of magnetic phases in the honeycomb quantum magnet $\mathrm{Na_3Ni_2SbO_6}$ studied by dilatometry and high-frequency ESR. *Phys. Rev. B* **2017**, *95*, No. 214414.

(59) Goldberg, D. P.; Telser, J.; Krzystek, J.; Montalban, A. G.; Brunel, L.-C.; Barrett, A. G. M.; Hoffman, B. M. EPR Spectra from "EPR-Silent" Species: High-Field EPR Spectroscopy of Manganese(III) Porphyrins. *J. Am. Chem. Soc.* **1997**, *119*, 8722−8723.

(60) Barra, A.-L.; Debrunner, P.; Gatteschi, D.; Schulz, C. E.; Sessoli, R. Superparamagnetic-like behavior in an octanuclear iron cluster. *Europhys. Lett.* **1996**, *35*, 133−138.

(61) Ahmed, N.; Sharma, T.; Spillecke, L.; Koo, C.; Ansari, K. U.; Tripathi, S.; Caneschi, A.; Klingeler, R.; Rajaraman, G.; Shanmugam, M. Probing the Origin of Ferro-/Antiferromagnetic Exchange Interactions in Cu(II)−4f Complexes. *Inorg. Chem.* **2022**, *61*, 5572−5587.

(62) Arneth, J.; Li, X.; Braun, J.; Paul, S.; Schulze, M.; Anson, C. E.; Wernsdorfer, W.; Powell, A. K.; Klingeler, R. The Interplay of Single Ion Anisotropy and Magnetic 3d-4f Interactions in $\mathrm{V_2^{III}Ln_2^{III}}$ Butterfly Complexes. *ChemistryEurope* **2025**, *3*, No. e202500011, DOI: 10.1002/ceur.202500011.

(63) Stoll, S.; Schweiger, A. EasySpin, a comprehensive software package for spectral simulation and analysis in EPR. *J. Magn. Reson.* **2006**, *178*, 42−55.

(64) Becke, A. D. A New Mixing of Hartree−Fock and Local Density-functional Theories. *J. Chem. Phys.* **1993**, *98*, 1372−1377.

(65) Caldeweyher, E.; Bannwarth, C.; Grimme, S. Extension of the D3 Dispersion Coefficient Model. *J. Chem. Phys.* **2017**, *147*, No. 034112.

(66) Caldeweyher, E.; Ehlert, S.; Hansen, A.; Neugebauer, H.; Spicher, S.; Bannwarth, C.; Grimme, S. A Generally Applicable Atomic-Charge Dependent London Dispersion Correction. *J. Chem. Phys.* **2019**, *150*, No. 154122.

(67) Balasubramani, S. G.; Chen, G. P.; Coriani, S.; et al. TURBOMOLE: Modular Program Suite for Ab Initio Quantum-Chemical and Condensed-Matter Simulations. *J. Chem. Phys.* **2020**, *152*, No. 184107.

(68) *TURBOMOLE V7.7 2022: A Development of University of Karlsruhe and Forschungszentrum Karlsruhe GmbH; Since 2007.*

(69) van Wüllen, C. Relation between Different Variants of the Generalized Douglas-Kroll Transformation through Sixth Order. *J. Chem. Phys.* **2004**, *120*, 7307−7313.

(70) van Wüllen, C.; Michauk, C. Accurate and Efficient Treatment of Two-Electron Contributions in Quasirelativistic High-Order Douglas-Kroll Density-Functional Calculations. *J. Chem. Phys.* **2005**, *123*, No. 204113.

(71) Meier, U.; Staemmler, V. An Efficient First-Order CASSCF Method Based on the Renormalized Fock-operator Technique. *Theor. Chim. Acta* **1989**, *76*, 95−111.

(72) Zong, R.; Wang, D.; Hammitt, R.; Thummel, R. P. Synthetic Approaches to Polypyridyl Bridging Ligands with Proximal Multidentate Binding Sites. *J. Org. Chem.* **2006**, *71*, 167−175.

(73) Peng, D.; Middendorf, N.; Weigend, F.; Reiher, M. An Efficient Implementation of Two-Component Relativistic Exact-Decoupling Methods for Large Molecules. *J. Chem. Phys.* **2013**, *138*, 184105.

(74) Arneth, J.; Pachl, C.; Greif, G.; Beier, B.; Roesky, P. W.; Fink, K.; Klingeler, R. Towards Understanding Prolate 4 Monomers: Numerical Predictions and Experimental Validation of Electronic Properties and Slow Relaxation in a Muffin-Shaped $\mathrm{Er^{III}}$ Complex.

July 21, 2025, arXiv:2507.15547. arXiv.org e-Print archive. https://arxiv.org/abs/2507.15547 (accessed Jan 02, 2026).